scientific reports

Check for updates

OPEN

Carbon minibeam radiation therapy results in tumor growth delay in an osteosarcoma murine model

Annaïg Bertho[1,2], Christian Graeff[3], Ramon Ortiz[1,2], Maria Giorgi[1,2], Christoph Schuy[3], Marjorie Juchaux[1,2], Cristèle Gilbert[1,2], Julie Espenon[1,2], Julius Oppermann[3], Olga Sokol[3], Walter Tinganelli[3] & Yolanda Prezado[1,2,4,5,6]✉

Despite remarkable advances, radiation therapy (RT) remains inefficient for some bulky tumors, radioresistant tumors, and certain pediatric tumors. Minibeam radiation therapy (MBRT) has emerged as a promising approach, reducing normal tissue toxicity while enhancing immune responses. Preclinical studies using X-rays and proton MBRT have demonstrated enhanced therapeutic index for aggressive tumor models. Combining MBRT's advantages of spatial dose fractionation with the physical and biological benefits of carbon ions could be a step further toward unleashing the full potential of MBRT. This study aims to perform the first in vivo study of local and systemic responses of a subcutaneous mouse osteosarcoma (metastatic) model to carbon MBRT (C-MBRT) versus conventional carbon ion therapy (CT). Irradiations were conducted at the GSI Helmholtz Centre in Germany using 180 MeV/u ^{12}C ions beam. All irradiated animals received an average dose (20 Gy) and displayed a significant and similar tumor growth delay in addition to a decreased metastasis score compared to the non-irradiated group. In the C-MBRT group, 70% of the tumor volume received the valley dose, which is a very low dose of 1.5 Gy. The remaining 30% of the tumor received the peak dose of 105 Gy, resulting in an average dose of 20 Gy. These results suggest that C-MBRT triggered distinct mechanisms from CT and encourage further investigations to confirm the potential of C-MBRT for efficient treatment of radioresistant tumors.

Keywords Minibeam radiation therapy, Carbon ions, Carbon therapy, Carbon minibeam radiation therapy (C-MBRT), Radioresistant tumor, Osteosarcoma

Radiotherapy (RT) is a cornerstone of cancer treatment. However, the dose tolerances of normal tissues still compromise an effective treatment of bulky tumors, radioresistant tumors, and certain pediatric cancers, among others. Therefore, finding novel approaches leading to healthy tissue protection is of utmost importance and especially critical in radioresistant tumors.

Minibeam radiation therapy (MBRT) is an unconventional approach that uses highly modulated dose distributions[1]. This spatially fractionated radiotherapy (SFRT) technique employs submillimetric (0.5–1.0 mm-wide) beams spaced by approximately 1.0 to 4.0 mm. Numerous preclinical studies with X-rays and proton MBRT have shown a very significant increase in normal tissue tolerances[2–8] as well as tumor control in aggressive tumor models, such as gliomas[9–12]. The successful results of the first veterinary clinical trials in *de novo* glioma-bearing dogs[13] and the outcome of the treatments of the first two MBRT patients[14] confirm the therapeutic interest of this technique.

[1]Institut Curie, CNRS UMR3347, Inserm U1021, Signalisation Radiobiologie et Cancer, Université PSL, 91400 Orsay, France. [2]CNRS UMR3347, Inserm U1021, Signalisation Radiobiologie et Cancer, Université Paris-Saclay, 91400 Orsay, France. [3]Biophysics Department, GSI Helmholtzzentrum für Schwerionenforschung, Darmstadt, Germany. [4]New Approaches in Radiotherapy Lab, Center for Research in Molecular Medicine and Chronic Diseases (CIMUS), Instituto de Investigación Sanitaria de Santiago de Compostela (IDIS), University of Santiago de Compostela, 15706 Santiago de Compostela, A Coruña, Spain. [5]Oportunius Program, Galician Agency of Innovation (GAIN), Xunta de Galicia, Santiago de Compostela, A Coruña, Spain. [6]Institut Curie Centre de Recherche, Rue Henri Becquerel, 91410 Orsay, France. ✉email: yolanda.prezado@curie.fr

Combining MBRT with heavy ions, particularly carbon ions, offers several advantages. On one hand, carbon ions provide higher dose conformality than photons and protons[13]. Their high linear energy transfer (LET), results in an increased relative biological effectiveness (RBE). A RBE of 1.1 is used with protons[14], while a RBE between 1.2 and 3.5 was measured with carbon ion beams in preclinical studies[15]. This increased RBE could lead to enhanced antitumor efficacy[13]. Moreover, carbon ions have a low oxygen enhancement ratio (ratio of the dose producing similar effects (cell death) in hypoxic and normoxic conditions), being more effective in killing hypoxic tumor cells. Furthermore, carbon ions induced a more robust immune response than photons[16]. This could lead to synergistic effects with the efficient and fast antitumor immune response observed in MBRT[17]. Finally, the reduced lateral scattering of carbon ions with respect to photons and protons results in higher Bragg peak-to-entrance dose ratio and sharper minibeam lateral dose profiles, favoring normal tissue sparing[18].

Carbon MBRT (C-MBRT) was explored in a first biological experiment[19], where only one rabbit brain was irradiated with several arrays of 130 MeV/u 300-µm-wide ^{12}C beams interlacing at the target, showing a reduced impact on the non-targeted tissues. Some pioneer dosimetry studies showed the potential interest of the technique[18,20]. However, long-term follow-up, statistically significant data, tumor efficacy studies, and dose-escalation studies in clinical beams are needed to confirm its clinical potential.

In this study, we investigate the tumor control efficacy of C-MBRT in an osteosarcoma murine model for the first time. This study investigated the potential synergy between carbon ions and MBRT to trigger a local and systemic immune response to reach tumor control and compared it to conventional carbon therapy.

Materials and methods

Ethical statement

The experiment was conducted in accordance with German federal law and with the approval of the Hessen Animal Ethics Committee (Project license 0050724-1-7). 8 weeks old male C3H/He mice (Charles River Laboratories, Freiburg, Germany) were used. The present study is reported in accordance with ARRIVE guidelines.

Tumor inoculation

1×10^6 LM8 mouse osteosarcoma cells, originating from C3H/He mice (Riken BioResource Center, Japan, RRID: CVCL_6669), in 20µL of PBS buffer solution were subcutaneously injected into one of the mice's posterior limbs, one week before irradiation. On the day of the irradiation, the average tumor volume was 229,05 mm^3. The animals included in the study had tumor diameter in the direction perpendicular to the beam direction large enough so that at least the tumor is irradiated with 3 minibeams (around 10 mm). Furthermore, this osteosarcoma model is known to generate metastases in the lung[21].

Irradiations and dosimetry

Carbon ion irradiation was performed using the pencil beam scanning system at the heavy-ion synchrotron (SIS18) at GSI Helmholtz Centre for Heavy Ion Research (Darmstadt, Germany). The ^{12}C beam energy was 180 MeV/u with an energy spread around 0.1%. The animals were irradiated in the plateau region.

The animals were distributed in three experimental groups, based on the tumor volume on the day of the irradiation (each group had the same mean tumor volume): a non-irradiated group ($n = 8$), a conventionally irradiated group (Carbon therapy, CT, $n = 9$), and a group receiving C-MBRT ($n = 10$). One animal was excluded due to small tumor volume. Each group was clearly identified on the cage at the time of irradiation. During irradiation, the mice were anesthetized with 1.5% isoflurane and immobilized vertically on the treatment bed.

The spatial fractionation of the beam was obtained using a multislit 3 cm-thick brass collimator. The irradiation was performed with 6 vertical slits of 500 ± 50 µm width and 50 mm height, spaced by a center-to-center (ctc) distance of 3.6 mm[22].

Radiochromic films were placed on the mice's skin for quality control. The tumor area was highlighted in each film to get the approximative geometrical distribution of the peak and valley regions in the irradiation field. In the C-MBRT group, the tumor received 3 mini beams, meaning that more than half of the tumor received only the valley dose (Fig. 1).

Experimental dosimetry of C-MBRT was performed using a two-step protocol as in previous MBRT studies[23]. Absolute dosimetry was performed with an ionization chamber (PTW 30013 Farmer ionization chamber (IC)) in broad beam conditions (6×6 cm^2 seamless field) placed at the isocenter of the room, 1 cm depth in a solid water (RW3) phantom. Relative dosimetry in MBRT employed a microdiamond detector (PTW 60019) and radiochromic films (GAFchromic™ EBTXD and OrthoChromic™ OC-1), as done in previous studies[20]. Both detectors were calibrated in the carbon beam. The microdiamond was calibrated, placing it in the same configuration as for C-MBRT measurements, i.e., on edge. Since the measurements were performed at the entrance of the plateau region, no significant quenching effects are expected[20].

Measurements were performed at 1 cm depth in a PMMA phantom of $10 \times 10 \times 2$ cm (Fig. 1a). The measurement point was at the isocenter of the room. The distance between the collimator exit and the phantom entrance was 1.5 cm.

The delivery system used was a research version of the Centro Nazionale di Adroterapia Oncologica (CNAO) dose delivery system[24,25]. The beam was monitored by parallel plate ICs read out at 1 MHz, calibrated daily to a Farmer chamber setup. Dosimetry accuracy for high-dose, uniform plans (before the collimator) should be well below the requested 5%, more likely in the order of 1%.The experimental measurements were compared to the dose distributions calculated by Monte Carlo simulation (TOPAS version 3.7 based on GEANT4 version 4.10.06.p03). The modular physics list type was used, including the 7 modules g4em-standard opt4, g4h-phy QGSP BIC HP, g4decay, g4ion-binarycascade, g4h-elastic HP, g4stopping and g4radioactivedecay[26,27]. A range cut value of 0.01 mm for all particles was used. Inside the scorer, a range cut of 0.005 mm was used for gamma,

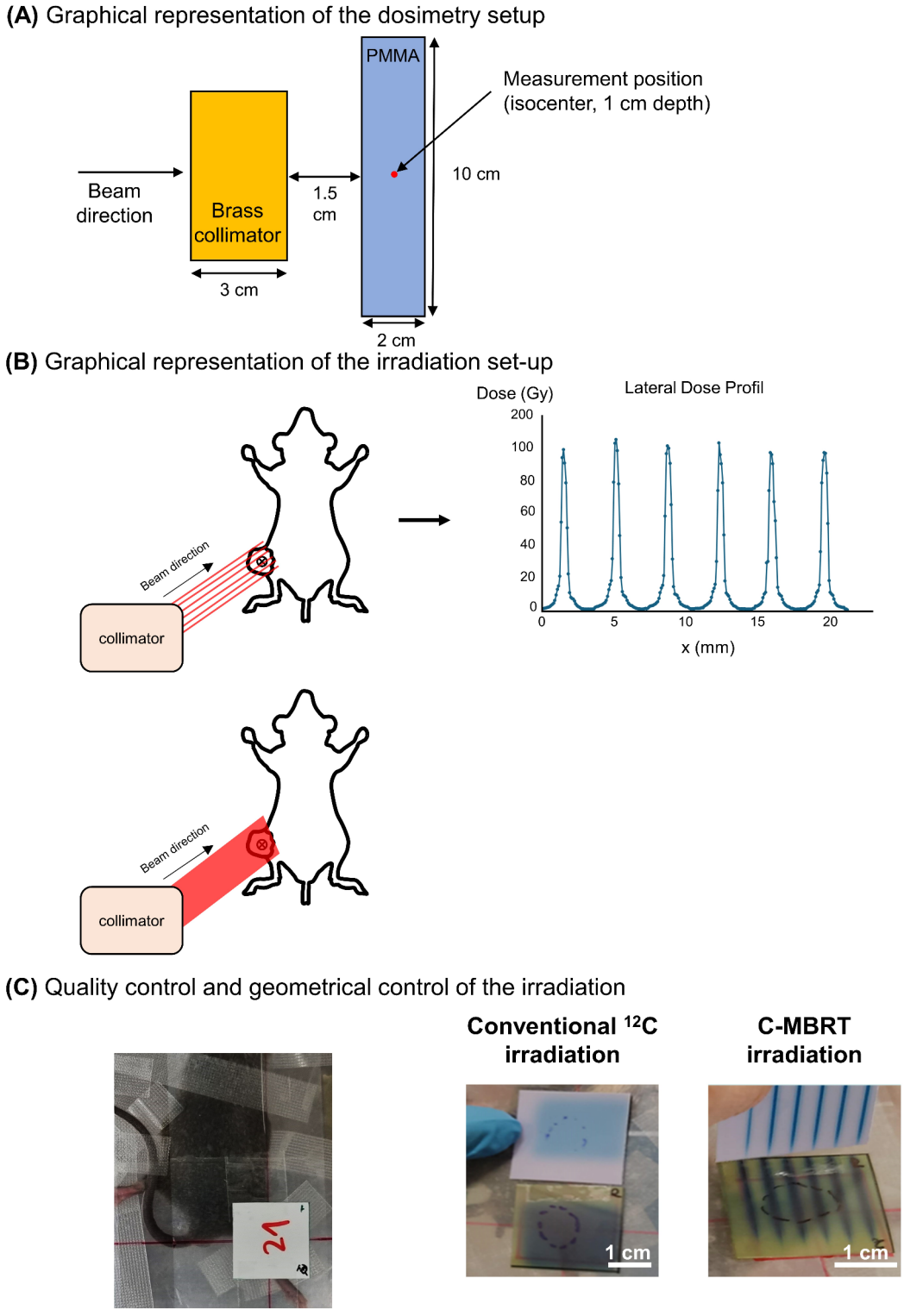

Fig. 1. Design of the experimental set-up. (**A**) Graphical representation of the radiation set-up used in this study. Mice were irradiated vertically. (**B**) Radiographic films were placed on the mice's skin at the beam exit for quality control. The films outlined the tumor to give the geometrical distribution of peaks and valleys in the C-MBRT group.

electron, positron, and proton. The primary particles employed were ~10^9 ^{12}C ions, and the global uncertainty, calculated as the average statistical uncertainty of voxels with a dose higher than 50% of the maximum dose, was < 1%. The GSI beam was simulated using the Emittance source type with the distribution attribute set to BiGaussian. Table 1 shows the beam source parameters employed provided by the Biophysics department of GSI.

E (MeV/U)	ΔE (%)	σ_x (mm)	σ_y (mm)	σ_{x^2} (mrad)	σ_{y^2} (mrad)	r_{xx^2}	r_{yy^2}
180	0.1	4.8	5.4	0.1	0.1	0	0

Table 1. Beam source parameters of emittance source type with two-dimensional elliptical Gaussian distributions per axis as tuned at GSI for the experiment (provided by the Biophysics department). E refers to the initial energy, ΔE to the energy spread, σ_x and σ_y to the standard deviation of the Gaussian that describes the spread of particle positions in both directions perpendicular to the beam direction, σ_{x^2} and σ_{y^2} to the spread in the momentum trajectory, and r_{xx^2} and r_{yy^2} to the correlation coefficient of the beam ellipses.

	PVDR	FWHM (mm)
Monte Carlo simulations	65.7 ± 0.1	0.50 ± 0.05
Microdiamond	70 ± 4	0.54 ± 0.05
Film	67 ± 4	0.51 ± 0.05

Table 2. PVDR and FWHM measured at 1 cm depth in a PMMA phantom.

Focal spots sizes were measured in air, at the isocenter, while divergence parameters were estimated based on a prior experiment[28].

Using the TOPAS scorer DoseToMaterial, the dose was evaluated at 1 cm depth in the PMMA phantom in voxels of $0.005 \times 0.2 \times 0.1$ cm^3.

Table 2 shows the C-MBRT irradiation characterization in terms of peak-to-valley dose ratio (PVDR) and full width half at maximum (FWHM). A global good agreement was obtained.

The dose prescription was 20 ± 1 Gy at 1 cm depth. In C-MBRT, this corresponds to peak and valley doses of 105 ± 6 Gy and 1.5 ± 0.1 Gy, respectively. This dose was chosen based on a previous study, demonstrating the healthy tissue-sparing effect of combining heavy ions with MBRT[29]. Figure 1 depicts the irradiation setup.

Animal follow-up

After irradiation, mice were monitored for 28 days for tumor growth and overall health conditions. Tumor sizes were measured 3 times a week using a digital caliper. Any animals reaching any of the endpoints (weight loss > 20%, tumor size in any dimension > 15 mm) were humanely euthanized. Tumors had approximately a hemi-ellipsoid shape. The tumor volume V was calculated from the measured length (a), width (b), and depth (c) with the formula: $V = \pi \times \left(\frac{a \times b \times c}{6}\right)$.

Histopathological analysis

At the end of the study, the mouse tumors and lungs were sampled and fixed in a zinc-formalin fixative solution (Sigma-Aldrich). Samples were embedded in paraffin, and 4 µm-thick paraffin tissue sections were cut. Sample processing has been performed at a certified histopathology core facility.

Immunohistochemistry analysis was performed using an antibody against Ki67 (MIB-5, 1:50, M7248, Dako CA, United States, RRID: AB_2142378), a proliferation marker followed by a secondary biotinylated antibody (Biotinylated Goat anti-mouse, 1:400, E0433, Dako CA, United States, RRID: AB_2687905). Saturation and permeabilization were performed using SmartBlock (113 500, Candor, Germany) and 0.25% Triton, unmasking with pH6 citrate buffer. Ki-67 positive cells were counted and normalized to the tumor area.

Tumor sections were stained with an antibody against CD8 (EPR21769, ab217344, Abcam, United Kingdom, RRID: AB_2890649), a marker of T cells, followed by a secondary biotinylated antibody (Goat anti-rabbit IgG, biotin conjugate, Ozyme, France, RRID: RRID: AB_3661653). Unmasking was performed with pH6 citrate buffer, and saturation using 5% Bovine Serum Albumin (BSA, A7030, Sigma-Aldrich, MO, United States) and 5% donkey serum (D9663, Sigma-Aldrich, MO, United States) in a solution of phosphate-buffered saline (PBS) and 2.5% Tween 20 (P1379, Sigma-Aldrich, MO, United States). The area of CD8 + staining was quantified and normalized to the section area using ImageJ software. 3 slides per sample were quantified. The same previously published approach was used[30] To quantify the CD8 + staining (brown staining) within the tumor area, first, RGB images were split into red, green, and blue channels. Then, the blue and red channels were inverted to obtain a black background. Second, an AND operation between these two channels was computed. Binary close operations followed by a fill hole produce a solid mask of the tumor. The area corresponding to the brown staining is determined by computing the ratio of red and green channels. Then, all pixels above a ratio of 1.13 are considered brown staining and used to create a mask of staining (applying the Yen thresholding method). The area of the tumor is determined on the mask of the tumor, and the area of brown pixels is determined only in the area covered by the mask of the tumor. In the end, the % of brown staining contained in the tumor is calculated.

For both staining, a negative control was performed by omitting the primary antibody incubation step to verify the specificity of the primary antibody. The sections were incubated with the secondary antibody alone.

Lung samples were sequentially cut to cover the whole lung volume and stained with hematoxylin, eosin, and saffron (HES) for metastasis quantification. Samples were digitalized on Zeiss Imager Z2 and Metasystems scanner using Metafer4 V3.12.9 and Vslide v1.1.115 softwares at magnification ×20. Images were quantitatively

and automatically analyzed using the QuPath Software[31–33]. QuPath was trained for tissue and tumor detection using the pixel classifier. First, color deconvolution was applied automatically, separating hematoxylin, eosin, and residual channels when images were uploaded to QuPath. Then, the tissue slice is automatically detected on each image by applying a pixel classifier. The pixel classifier was obtained by using a threshold value set at 225 Gy levels working at high resolution (downsample = 4) on the average (mean of the RGB) channel after a Gaussian filter (sigma 3). After detection, the final tissue annotation is created by excluding objects smaller than 100,000,000 pixels^2 and small holes in the tissue lower than 1,000,000 pixels^2. Then, inside the tissue annotation, a pixel classifier based on machine learning was used to recognize metastasis regions automatically. To improve the robustness of the pixel classifier, a training image composed of 42 tissue regions (1000*1000 pixels) was created from 7 images. The training dataset was manually annotated to classify pixels into 2 categories: tumor and stroma. Then, a random tree classifier was trained on the hematoxylin and eosin channels with the selection of 3 features (gaussian, Laplacian of Gaussian, weighted deviation) at 3 different scales (1, 4, and 8) at high resolution (downsample = 4). Finally, metastasis areas lower than 12,000 pixels^2 and holes size under 12,000 pixels^2 are removed from the detection. At the end, the percentage of metastasis in the tissue and the total tissue area are extracted. All histopathological assessments were performed blinded.

Statistical analysis

Statistical analysis was performed using one-way or two-way ANOVA and Tukey's multiple comparisons test. These statistical analyses were performed on GraphPad Prism 10 (GraphPad Software, CA, United States). Data is expressed as mean ± standard error of the mean. The sample size was determined using G*power software.

Results

Tumor growth and toxicity

Slight alopecia appeared on the irradiated region from 12 days post-irradiation and persisted until the end of the study in all irradiated animals (Fig. 2A). No skin toxicities were observed.

Figure 2B reports the average tumor volume as a percentage of the initial tumor volume. Both irradiation modes resulted in a significant tumor growth delay with respect to the non-irradiated controls. Tumor control was similar between C-MBRT and CT, despite more than 70% of the tumor volume in MBRT receiving very low (valley) doses of 1.5 Gy, and less than 30% of tumor volume receiving a very high (peak) dose of 105 ± 6 Gy (Fig. 1). It is important to note that the dose of 1.5 Gy is considered a very low dose compared to the median total dose delivered to treat radioresistant osteosarcoma in clinics, which is 66 Gy[34] deliver in 2 Gy fractions, 5 times a week. It is also low compared to the 20 Gy delivered homogeneously in the whole tumor volume in the CT group. Moreover, the mean dose of 20 Gy was chosen to avoid the development of radiation-induced skin toxicities, which would have compromised the study of the tumor control.

Histopathological analysis

At the end of the study, the tumor cell proliferative state was quantified using Ki67 staining. Figure 3 shows the normalized Ki67-positive cell counts among the tumors. Ki67 is a nuclear protein expressed in proliferative cells. No significant differences in the number of Ki67-positive tumor cells were observed among the groups. Dose escalation, made possible with C-MBRT by reducing damage to healthy tissue, may be necessary to decrease the proliferative state of the tumor and achieve definitive tumor control.

T-cell infiltration into the tumor was quantified using CD8 staining. Figure 4 shows the percentage of CD8-positive T-cell staining among the tumors at 28 days post-irradiation, the end of the study. Compared to the controls, a significant CD8-positive T-cell infiltration in the tumor is observed in both irradiated groups. However, at this late time point, CT results in a higher proportion of CD8-positive T cells in the tumor than C-MBRT which suggests a more sustained immune response.

Given that the LM8 osteosarcoma tumor model is known to form spontaneous lung metastases, we determined metastasis scores among the experimental groups. Figure 5A shows the macroscopic appearance of the whole lung at the end of the study. All the experimental groups displayed macroscopic lung metastasis. Lung metastases were scored on HES-stained sections (Fig. 5B,C). C-MBRT and CT irradiations decreased the metastasis score compared to the non-irradiated controls (fold-change of 0.80 and 0.15, respectively). CT irradiations also decreased the metastasis score compared to the C-MBRT (fold-change of 0.19).

Discussion

Despite remarkable progress in the radiotherapy domain, some radioresistant tumors remain without effective treatment. Unconventional techniques activating distinct biological mechanisms and leading to toxicity reduction and more favorable immune and vascular effects could be pivotal innovations for those difficult-to-treat cases. Along this line, MBRT is a technique that employs a distinct dose delivery method and exploits the different radiobiology triggered by spatial dose heterogeneity[1]. X-rays and protons MBRT have already demonstrated an important widening of the therapeutic window for aggressive tumor models, such as gliomas[9,10,35]. Combining MBRT and carbon ions could bring further advantages related to heavy ions' physical and biological characteristics13.

Previous dosimetry evaluations of C-MBRT suggested favorable dose distributions for normal tissue sparing thanks to the reduced lateral scattering of heavy ions[18]. However, this also implies that highly heterogeneous dose distributions are also to be expected in the target. While tumor control has been obtained with heterogeneous dose distributions in X-rays and proton MBRT[10,12], the peak-to-valley dose ratio in C-MBRT is 5–7 times higher. The distributions are, therefore, more heterogeneous. To the best of our knowledge, this is the first evaluation of tumor control following C-MBRT.

(A) Alopecia observed on the beam path

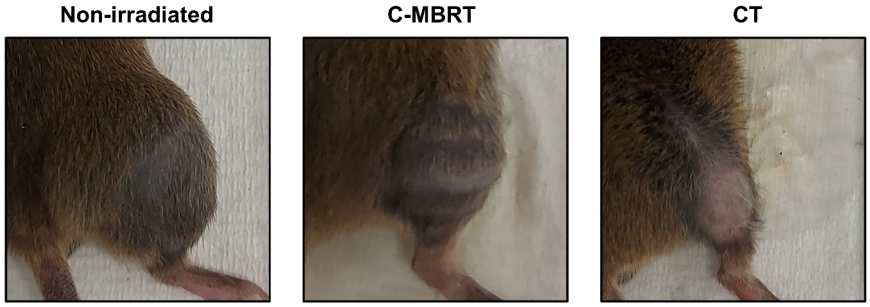

(B) Tumor growth of LM8 osteosarcoma after ^{12}C ion irradiations

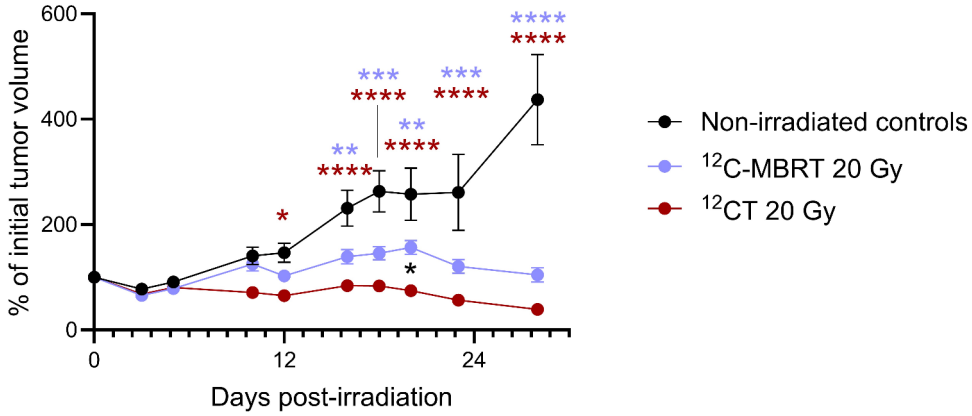

(C) Two-Way ANOVA of Tumor growth

Source of variation	F(DFn. DFd)	p value
Interaction	F (18. 228) = 8.986	p<0.0001
Irradiation modality	F (9. 228) = 11.10	p<0.0001
Days	F (2. 228) = 87.71	p<0.0001

Tukey's multiple comparisons test	Controls vs C-MBRT	Controls vs CT	C-MBRT vs CT
Day 0	>0.9999 (ns)	>0.9999 (ns)	>0.9999 (ns)
Day 3	0.9207 (ns)	0.9523 (ns)	0.9957 (ns)
Day 5	0.9045 (ns)	0.9345 (ns)	0.997 (ns)
Day 10	0.8617 (ns)	0.0622 (ns)	0.1321 (ns)
Day 12	0.3078 (ns)	0.0232 (*)	0.378 (ns)
Day 16	0.0068 (**)	<0.0001 (****)	0.1204 (ns)
Day 18	0.0003 (***)	<0.0001 (****)	0.0697 (ns)
Day 20	0.0042 (**)	<0.0001 (****)	0.0102 (*)
Day 23	<0.0001 (***)	<0.0001 (****)	0.0596 (ns)
Day 28	<0.0001 (****)	<0.0001 (****)	0.0512 (ns)

Fig. 2. Clinical symptoms observed following C-MBRT and conventional ^{12}C irradiations. (**A**) Representative images of radiation-induced alopecia restricted to the irradiated area observed in the C-MBRT and CT groups, compared to the non-irradiated controls at 28 days post-irradiation. Mice limb were shaved before the tumor cell injection, explaining the slightly uneven fur growth in the non-irradiated control animals (**B**) Tumor growth curve of mice LM8 osteosarcoma after ^{12}C irradiations. C-MBRT and CT lead to similar tumor control. In black = non-irradiated controls; blue = C-MBRT irradiated group; and red = CT irradiated group. Data are presented as the mean ± Standard error of the mean (SEM) (**C**) Statistical analysis regarding tumor growth was done using Two-Way ANOVA and Tukey's multiple comparisons test. p-values < 0.05 were considered significant. *$p < 0.05$; **$p < 0.01$; ***$p < 0.001$; ****p-value < 0.0001.

(A) Proliferative state of the tumor cells

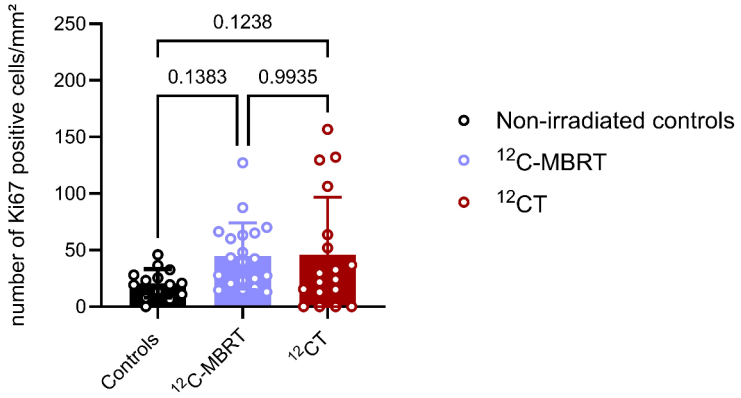

(B) Representative images of Ki67 staining in the tumor

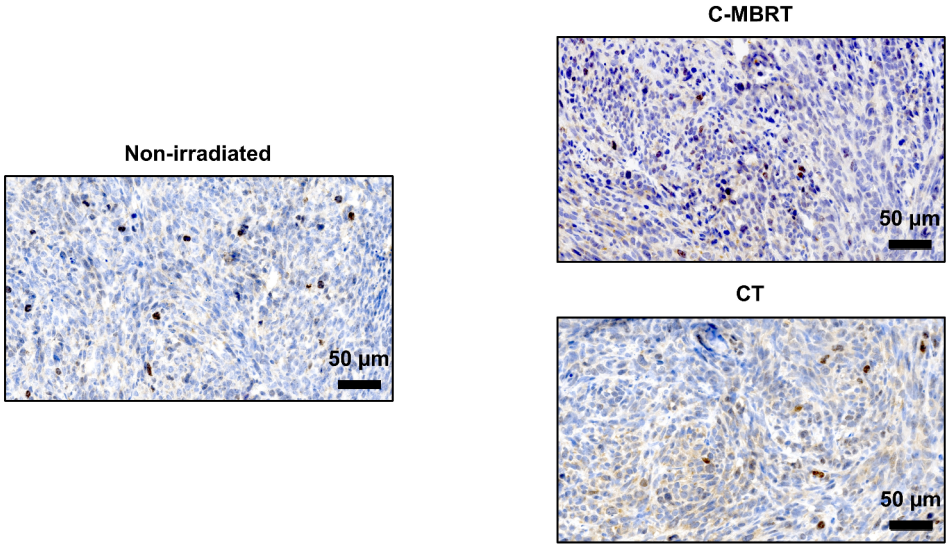

(C) One-Way ANOVA

One-Way ANOVA summary	p value	F (DFn, DFd)
Irradiation modality	0.0958	F (2, 49) = 2.461

Tukey's multiple comparisons test	Adjusted P Value
Non-irradiated controls vs. ¹²C-MBRT	0.1383
Non-irradiated controls vs. ¹²CT	0.1238
¹²C-MBRT vs. ¹²CT	0.9935

Fig. 3. LM8 osteosarcoma proliferative state following C-MBRT and CT, at the end of the study. (**A**) Proliferative state of the tumor cells. The graphic represents the density of Ki67-positive cells in the tumor: in black = non-irradiated controls; in blue = C-MBRT irradiated group; and red = CT irradiated group. Data are represented as the mean ± Standard Deviation (SD). (**B**) Representative images of Ki67 staining in the tumor, following C-MBRT and CT, compared to the non-irradiated controls. (**C**) Statistical analysis regarding Ki67-positive cell density in the tumor was done using One-Way ANOVA and Tukey's multiple comparisons test. *p*-values < 0.05 were considered significant. **p* < 0.05; ***p* < 0.01; ****p* < 0.001; *****p*-value < 0.0001.

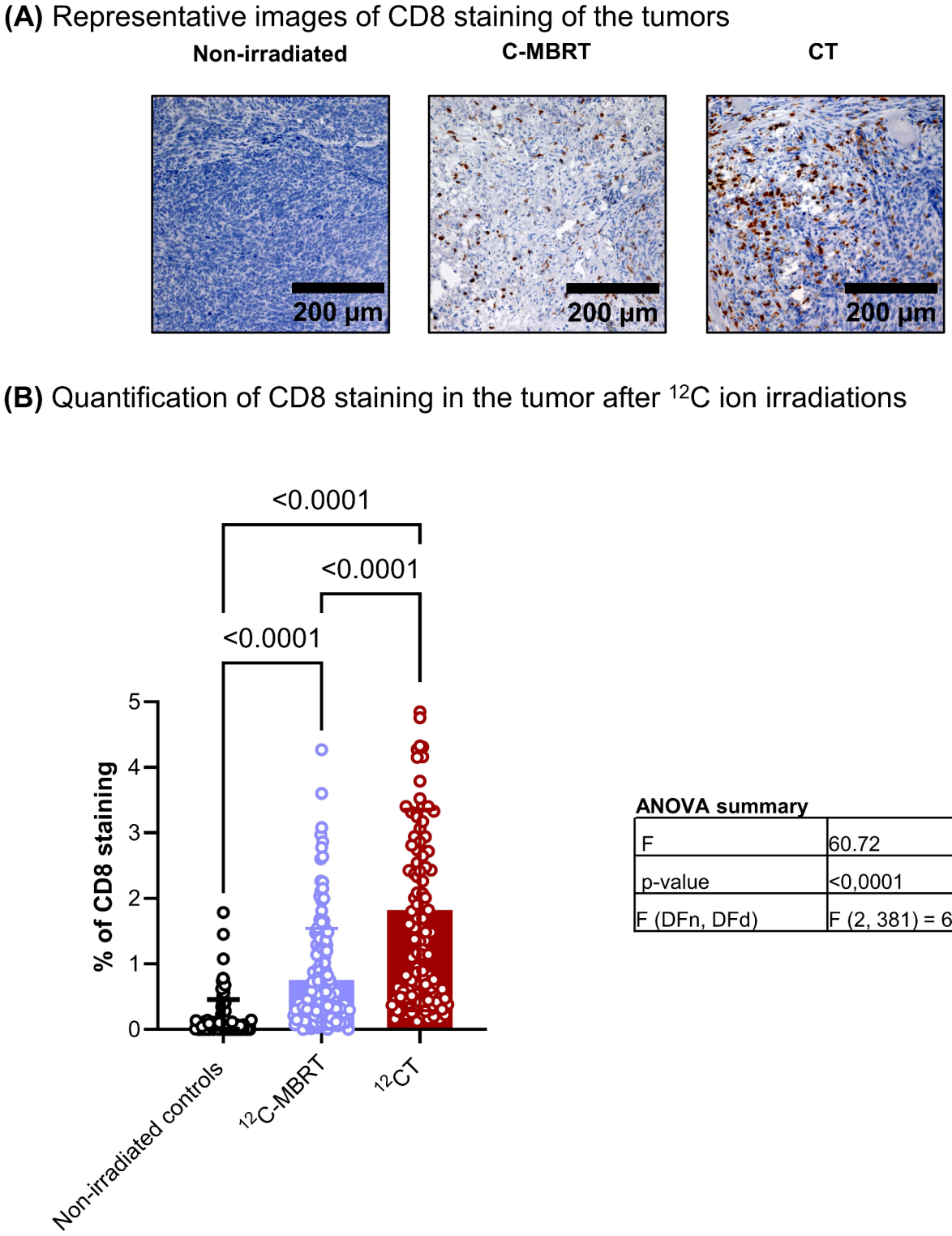

ANOVA summary

F	60.72
p-value	<0,0001
F (DFn, DFd)	F (2, 381) = 60.72

Fig. 4. T-cell infiltration of LM8 osteosarcoma following C-MBRT and CT, compared to the non-irradiated controls. (**A**) Representative images of CD8 staining of the tumors in the C-MBRT, CT, and non-irradiated groups. (**B**) CD8 positive T-cell infiltration of the tumor cells. The graphic represents the percentage of CD8-positive staining in the tumor section: in black = non-irradiated controls; in blue = C-MBRT irradiated group; and in red = CT irradiated group. Data are represented as the mean ± Standard Deviation (SD). Statistical analysis regarding CD8-positive cell density in the tumor was done using One-Way ANOVA and Tukey's multiple comparisons test. *p*-values < 0.05 were considered significant. **p* < 0.05; ***p* < 0.01; ****p* < 0.001; *****p*-value < 0.0001.

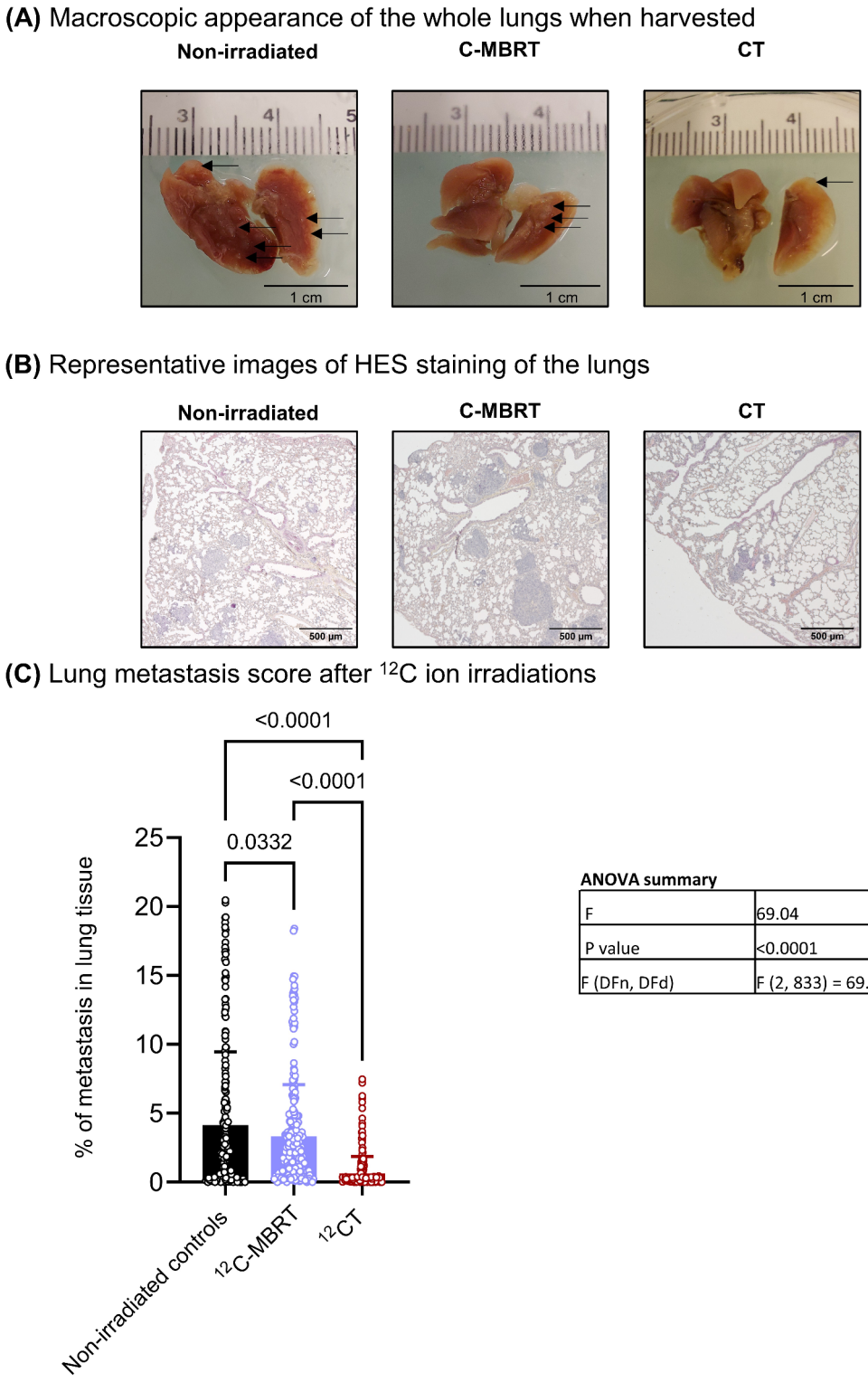

Fig. 5. LM8 osteosarcoma metastasis score following C-MBRT and CT, 28 days after irradiation. (**A**) Macroscopic aspect of the whole lungs at the end of the study. (**B**) Representative images of HES staining of the lungs. (**C**) The graphic represents the lung metastasis score: in black = non-irradiated controls; in blue = C-MBRT irradiated group; and red = CT irradiated group. Data are represented as the mean ± Standard Deviation (SD). Statistical analysis regarding the lung metastasis score was done using One-Way ANOVA and Tukey's multiple comparisons test. *p*-values < 0.05 were considered significant. **p* < 0.05; ***p* < 0.01; ****p* < 0.001; *****p*-value < 0.0001.

Osteosarcoma is the most common bone tumor in adolescents and young adults, with a 5-year survival rate of 65–70%. However, some patients develop resistance, relapse, or metastases, leading to a significantly reduced survival rate of 5–20%, highlighting the urgent need for improved treatments[36]. Osteosarcoma is known for its radioresistance, making it challenging to treat with conventional radiation therapy[34]. Advanced radiation therapies, such as SBRT and particle therapy, including carbon ion therapy, have shown promise in improving outcomes. Carbon ions, with their higher linear energy transfer (LET) and enhanced biological effect, combined with the healthy tissue preservation and antitumor immune response of MBRT, could offer potential benefits for radioresistant tumors like osteosarcoma.

The osteosarcoma model (C3H/He mice, LM8 cells) was chosen for its syngeneic nature and its high metastatic potential, allowing the study of local and systemic antitumor immunity in immunocompetent animals. Its metastatic nature reflects the clinical challenges of human osteosarcoma. Additionally, the LM8 model is intrinsically radioresistant; therefore, radiation therapy is considered inefficient in treating this type of tumor in clinical practice[34,37]. We aim to investigate whether combining MBRT and carbon ions could overcome this radioresistance.

This study observed a similar tumor growth delay when the same average dose was employed in C-MBRT and CT. In C-MBRT, 70% of the tumor volume received 1.5 Gy, which is a very low dose to be efficient against the tumor. This was achieved with the tumor receiving 3 mini beams (Fig. 1C). Recent studies suggest that the number of minibeams (as measured by the percentage of peak/valley widths) does not significantly influence tumor control[38]. However, dose heterogeneity has been associated with reduced immunosuppression[39] and favorable immune modulation[40]. This also highlights the need for further studies to evaluate the impact of dose heterogeneity on the tumor response.

It should be highlighted that the valley dose employed in this study is significantly lower than the one required in X-rays and proton MBRT to achieve a minimum tumor control (5–10 Gy)[12,41]. Therefore, our results suggest the activation of distinct mechanisms from a direct tumor cell death from radiation. In a recent in silico study, Masilela et al.[42]. assessed the free radical yields in both peak and valleys of different charged particle and MBRT combinations. In contrast to proton or helium MBRT, C-MBRT leads to a higher primary yield of $^{\cdot}OH$ radicals and a lower primary yield of H_2O_2 in the valleys than in the peaks. While the levels of $^{\cdot}OH$ are indicative of the indirect DNA damage[43], the level of H_2O_2 is implicated in non-targeted effects[44] and the potential immune response[45] observed in MBRT. These results point to an increased level of indirect DNA damage in the C-MBRT valleys compared to what would be suggested by the PVDR. Future research is necessary to fully explain these non-targeted cytotoxic effects and model their primary signaling mechanisms (e.g. reactive oxygen species and cytokine-like signaling pathways) in greater detail.

Previous results in X-rays MBRT[17] showed that T cells are key in the MBRT anti-tumor response. MBRT triggered an efficient CD8 + T cell infiltration at the tumor center 48 h after irradiation, compared to the non-irradiated controls and conventionally irradiated animals. While the current study was not designed to specifically assess the immune response after C-MBRT, an evaluation of CD8-positive T cells was performed 28 days after the irradiation. Despite the late time point, a significantly higher density of cytotoxic T cells was found in the tumors of the irradiated animals, independently of the irradiation mode (CT or C-MBRT, Fig. 4). The higher density of CD8-positive T cells in the CT group compared with the C-MBRT group 28 days after irradiation indeed suggests a positive correlation with a more sustained and efficient systemic immune response at the high dose used in CT. This sustained immune response might explain why, despite similar local tumor control in both irradiation modes, the systemic effects resulting in metastasis reduction were weaker in C-MBRT than in CT. Improved results could be expected by employing other configurations with narrower beam spacing and, therefore, a higher valley dose. Indeed, valley dose has been correlated to increased lifespan[38]. Some other strategies to improve results could be a dose escalation or a combination with immune checkpoint inhibitors.

While this pilot study focused on CD8 + T-cell infiltration and Ki67 proliferation to assess the efficacy of C-MBRT in tumor control, we acknowledge that a more comprehensive analysis, including a wider range of molecular and cellular markers (apoptosis, DNA damage, and other immune populations), is necessary to fully understand the biological responses and potential immune modulation triggered by C-MBRT.

Conclusion

The tumor control efficiency of C-MBRT was investigated, for the first time, in radioresistant murine osteosarcoma. C-MBRT achieves tumor control comparable to CT despite over 70% of the tumor receiving a low valley dose of only 1.5 Gy and less than 30% of tumor volume receiving a very high (peak) dose of 105 ± 6 Gy. This suggests the activation of distinct mechanisms beyond direct tumor cell death from radiation. However, CT induces a more sustained immune response. These observations highlight the potential of C-MBRT for effective tumor control with reduced damage to healthy tissue. Further optimization of the irradiation configuration or combining immune-checkpoint inhibitors could enhance its therapeutic efficacy.

Data availability

The raw data supporting this study's findings are available from the corresponding author, YP, upon reasonable request.

Received: 9 October 2024; Accepted: 24 February 2025
Published online: 01 March 2025

References

1. Prezado, Y. et al. Spatially fractionated radiation therapy: A critical review on current status of clinical and preclinical studies and knowledge gaps. *Phys. Med. Biol.* **69**(10), 1–21, 2024.
2. Dilmanian, F. A. et al. Interlaced x-ray microplanar beams: A radiosurgery approach with clinical potential. *Proc. Natl. Acad. Sci. U S A* **103** (25), 9709–9714 (2006).
3. Deman, P. et al. Monochromatic minibeams radiotherapy: From healthy tissue-sparing effect studies toward first experimental glioma bearing rats therapy. *Int. J. Radiat. Oncol. Biol. Phys.* **82** (4), e693–700 (2012).
4. Prezado, Y. et al. Tolerance to dose escalation in minibeam radiation therapy applied to normal rat brain: Long-term clinical, radiological and histopathological analysis. *Radiat. Res.* **184** (3), 314–321 (2015).
5. Prezado, Y. et al. Proton minibeam radiation therapy spares normal rat brain: Long-term clinical, radiological and histopathological analysis. *Sci. Rep.* **7** (1), 14403 (2017).
6. Prezado, Y. et al. Transfer of minibeam radiation therapy into a cost-effective equipment for radiobiological studies: A proof of concept. *Sci. Rep.* **7** (1), 17295 (2017).
7. Lamirault, C. et al. Short and long-term evaluation of the impact of proton minibeam radiation therapy on motor, emotional and cognitive functions. *Sci. Rep.* **10** (1), 13511 (2020).
8. Girst, S. et al. Proton minibeam radiation therapy reduces side effects in an in vivo mouse ear model. *Int. J. Radiat. Oncol. Biol. Phys.* **95** (1), 234–241 (2016).
9. Prezado, Y. et al. Tumor control in RG2 glioma-bearing rats: A comparison between proton minibeam therapy and standard proton therapy. *Int. J. Radiat. Oncol. Biol. Phys.* **104** (2), 266–271 (2019).
10. Sotiropoulos, M. et al. X-rays minibeam radiation therapy at a conventional irradiator: Pilot evaluation in F98-glioma bearing rats and dose calculations in a human Phantom. *Clin. Transl Radiat. Oncol.* **27**, 44–49 (2021).
11. Bertho, A. et al. First evaluation of temporal and spatial fractionation in proton minibeam radiation therapy of glioma-bearing rats. *Cancers (Basel)* **13**(19), 2–13, (2021).
12. Prezado, Y. et al. Proton Minibeam radiation therapy widens the therapeutic index for high-grade gliomas. *Sci. Rep.* **8** (1), 16479 (2018).
13. V. Kundapur, M. Mayer, R. N. Auer, A. Alexander, S. Weibe, M. J. Pushie, G. Cranmer-Sargison, Is Mini Beam Ready for Human Trials? Results of Randomized Study of Treating De-Novo Brain Tumors in Canines Using Linear Accelerator Generated Mini Beams. *Radiat. Res.* **198**, 162–171 (2022).
14. Grams, M. P. et al., Minibeam Radiation Therapy Treatment (MBRT): Commissioning and First Clinical Implementation. *Int. J. Radiat. Oncol. Biol. Phys.* **120**(5), 1423–1434. https://doi.org/10.1016/j.ijrobp.2024.06.035 (2024).
15. Tinganelli, W. & Durante, M. Carbon ion radiobiology. *Cancers (Basel)*. **12**(10), 2–37 (2020).
16. Zhou, H. et al. Carbon ion radiotherapy triggers Immunogenic cell death and sensitizes melanoma to anti-PD-1 therapy in mice. *Oncoimmunology* **11** (1), 2057892 (2022).
17. Bertho, A. et al. Evaluation of the role of the immune system response following minibeam radiation therapy. *Int. J. Radiat. Oncol. Biol. Phys.*, (2022).
18. González, W., Peucelle, C. & Prezado, Y. Theoretical dosimetric evaluation of carbon and oxygen minibeam radiation therapy. *Med. Phys.* **44** (5), 1921–1929 (2017).
19. Dilmanian, F. A. et al. Interleaved carbon minibeams: An experimental radiosurgery method with clinical potential. *Int. J. Radiat. Oncol. Biol. Phys.* **84** (2), 514–519 (2012).
20. Martínez-Rovira, I. et al. Carbon and oxygen minibeam radiation therapy: An experimental dosimetric evaluation. *Med. Phys.* **44** (8), 4223–4229 (2017).
21. Helm, A. et al. Reduction of lung metastases in a mouse osteosarcoma model treated with carbon ions and immune checkpoint inhibitors. *Int. J. Radiat. Oncol. Biol. Phys.* **109** (2), 594–602 (2021).
22. Voltz, L. et al. Investigating slit-collimator-produced carbon ion minibeams with high-resolution CMOS sensors. *Instruments* **7**, 20 (2003).
23. Prezado, Y. et al. Dosimetry protocol for the preclinical trials in white-beam minibeam radiation therapy. *Med. Phys.* **38** (9), 5012–5020 (2011).
24. Giordanengo, S. et al. The CNAO dose delivery system for modulated scanning ion beam radiotherapy. *Med. Phys.* **42** (1), 263–275 (2015).
25. Abdel-Wahab, M. et al. Radiotherapy and theranostics: A lancet oncology commission. *Lancet Oncol.* **25** (11), e545–e580 (2024).
26. Stengl, C. et al. Dosimetric study for breathing-induced motion effects in an abdominal pancreas Phantom for carbon ion mini-beam radiotherapy. *Med. Phys.* **51** (8), 5618–5631 (2024).
27. Régnier, E. et al. Re-irradiation of locally recurrent pediatric intracranial ependymoma: Experience of the French society of children's cancer. *Radiother Oncol.* **132**, 1–7 (2019).
28. Lis, M. et al. A facility for the research, development, and translation of advanced technologies for ion-beam therapies. *J. Instrum.*, **16**, 1–25 (2021).
29. Prezado, Y. et al. A potential renewed use of very heavy ions for therapy: Neon minibeam radiation therapy. *Cancers (Basel)* **13**(6), 1–14 (2021).
30. Morabito, M. et al. An autocrine ActivinB mechanism drives TGFβ/Activin signaling in group 3 medulloblastoma. *EMBO Mol. Med.* **11** (8), e9830 (2019).
31. Bankhead, P. et al. QuPath: open source software for digital pathology image analysis. *Sci. Rep.* **7** (1), 16878 (2017).
32. Igbo, B. T. et al. Immunohistochemical analyses of paraffin-embedded sections after primary surgery or trimodality treatment in esophageal carcinoma. *Clin. Transl Radiat. Oncol.* **36**, 106–112 (2022).
33. Deuss, E. et al. Standardized digital image analysis of PD-L1 expression in head and neck squamous cell carcinoma reveals intra- and inter-sample heterogeneity with therapeutic implications. *Cancers (Basel)*, **16**(11), 1–22 (2024).
34. Ducassou, A. et al. [Rôle of radiotherapy for sarcomas]. *Cancer Radiother* **25** (6–7), 598–602 (2021).
35. Lamirault, C. et al. Spatially modulated proton minibeams results in the same increase of lifespan as a uniform target dose coverage in F98-glioma-bearing rats. *Radiat. Res.* **194** (6), 715–723 (2020).
36. Isakoff, M. S. et al. Osteosarcoma: current treatment and a collaborative pathway to success. *J. Clin. Oncol.* **33** (27), 3029–3035 (2015).
37. Whelan, J. S. & Davis, L. E. Osteosarcoma, chondrosarcoma, and chordoma. *J. Clin. Oncol.* **36** (2), 188–193 (2018).
38. Fernandez-Palomo, C., Chang, S. & Prezado, Y. Should peak dose be used to prescribe spatially fractionated radiation therapy? A review of preclinical studies. *Cancers (Basel),* **14**(15), 1–13 (2022).
39. Potiron, S. et al. The significance of dose heterogeneity on the anti-tumor response of minibeam radiation therapy. *Radiother Oncol.* **201**, 110577 (2024).
40. Jagodinsky, J. C. et al. Intratumoral radiation dose heterogeneity augments antitumor immunity in mice and primes responses to checkpoint Blockade. *Sci. Transl Med.* **16** (765), eadk0642 (2024).
41. Guardiola, C. et al. Effect of X-ray Minibeam radiation therapy on clonogenic survival of glioma cells. *Clin. Transl Radiat. Oncol.* **13**, 7–13 (2018).
42. Masilela, T. A. M. & Prezado, Y. Monte Carlo study of the free radical yields in minibeam radiation therapy. *Med. Phys.*, (2023).
43. Weinberg, F., Ramnath, N. & Nagrath, D. Reactive oxygen species in the tumor microenvironment: an overview. *Cancers (Basel)* **11**(8), 1–20, (2019).

44. Zhou, Y. et al. Reactive oxygen species in vascular formation and development. *Oxid. Med. Cell. Longev.* **2013**, 374963 (2013).
45. Yang, Y. et al. Reactive oxygen species in the immune system. *Int. Rev. Immunol.* **32** (3), 249–270 (2013).

Acknowledgements
the results presented here are based on the experiment SBio08_Prezado "Heavy Ion Spatial Fractionated Radiotherapy" (Prezado, Yolanda et al.), which was performed in Cave M at the GSI Helmholtzzentrum fuer Schwerionenforschung (Darmstadt, Germany) in the frame of FAIR Phase-0.The authors warmly thank David Hardy, Magali Tichit, and Sara Loulizi (Histopathology Core Facility, Institut Pasteur, 75015 Paris, France) for supporting the histopathological analysis of stainings. The authors greatly acknowledge Cédric Messaoudi and Laetitia Besse from Multimodal Imaging Center - CNRS UAR2016 / Inserm US43 / Institut Curie / Université Paris-Saclay - for useful advice on image processing.

Author contributions
Project supervision: YP; Experimental design: YP, CGr; funding acquisition: YP; Data analysis: AB, YP; histopathological and IHC: AB; animals follow up: WT, OS, JO, JE, MJ, CG; Scientific discussions: YP, AB; irradiations and dosimetry: CGr, CS, RO, MG, YP, WT, JO, OS; manuscript writing: YP, AB.

Funding
This project has received funding from the European Union's Horizon 2020 research and innovation program under grant agreement No 101008548 (HITRI+). The research was also partially funded by the European Research Council (ERC) under the European Union's Horizon 2020 research and innovation program (grant agreement No 817908).

Declarations

Competing interests
The authors declare no competing interests.

Additional information
Correspondence and requests for materials should be addressed to Y.P.

Reprints and permissions information is available at www.nature.com/reprints.

Publisher's note Springer Nature remains neutral with regard to jurisdictional claims in published maps and institutional affiliations.